AIAA JOURNAL
Vol. 34, No. 7, July 1996

Analysis of Unsteady Supersonic Viscous Flows by a Shock-Fitting Technique

F. Nasuti* and M. Onofri†
University of Rome "La Sapienza," Rome 00184, Italy

An extension of Moretti's classical shock-fitting technique is proposed to solve complicated unsteady viscous flows. This version allows the automatic treatment of flow structures featuring triple points and shock interactions. A fitting of contact discontinuities has also been introduced for a number of problems. The fitting procedure is used with a Navier–Stokes solver based on the λ scheme. Validation tests for selected cases are presented.

Introduction

THE numerical treatment of shocks by floating shock-fitting techniques was introduced in the 1970s by Moretti.[1,2] The method explicitly assumes the shocks to be discontinuities of the flowfield, governed by the Rankine–Hugoniot relations. It basically relies on a one-dimensional approach, with the shock strength computed following the procedure reported in Ref. 3. Therefore, it can easily handle shocks approximately oriented along one of the directions of the families of coordinate lines. As a consequence, initially the fitting was limited to these shocks, considering only their intersections with the other family of coordinate lines.

Moretti introduced many improvements to his original version, including the ability to compute viscous flows,[4] and then proposed a generalized extension of the technique to fit shocks having any orientation with respect to the coordinate lines.[5] This approach was shown to be successful in many practical applications of supersonic flows.[5–7] Unfortunately, it requires a procedure to determine the local shock slope, which was not sufficiently robust, particularly when complicated shock interactions take place, or when many discontinuities are too close to one another. On the other hand, the quality of the results obtained prompted other attempts to be made to improve robustness.[8,9]

Although such efforts have not resulted yet in a satisfactory general version of the shock-fitting technique, renewed attention to possible improvements arose from its capability to compute accurately flow transients that are characterized by complex shock interactions. In such cases, the location and the speed of the moving shocks can be predicted precisely, without adding any computational cost, whereas to achieve solutions of comparable accuracy other methods need a specific handling of the discontinuities (like the use of very fine grids, or moving adaptive grids to be redefined at each integration step, or high-order schemes), which can eventually raise the computational time to impractical levels.

The aim of this paper is to present a further development of the methodology to predict unsteady behavior of both viscous and inviscid supersonic flows. An algorithm that integrates the Navier–Stokes equations written in nonconservative form, coupled to the fitting of shocks and contact discontinuities, is proposed. This method can be seen as a natural evolution of Moretti's original technique. In particular, it has been carried out by introducing modifications to the procedure proposed by Moretti,[5,10] with the extensions introduced to compute viscous flows.[11] Moreover, contact discontinuities are explicitly fitted and tracked. Thus, when the shock is close to a contact discontinuity, the smearing of the entropy jump that could affect the prediction of the shock propagation can be avoided.

A description of the new approach is reported, along with a review of the main aspects of the classical approach. Applications to selected test cases show the accuracy and the capability of the technique to solve steady and unsteady, inviscid and viscous supersonic flows.

Governing Equations

Following the pioneering theoretical work of Ref. 1, which analyzes the mathematical properties of the nonconservative form of Navier–Stokes equations written in terms of speed of sound a, velocity $\boldsymbol{v}$, and entropy s, the equation set is considered here in nondimensional variables as

$$\begin{cases} \dfrac{1}{\delta}\dfrac{\mathrm{D}a}{\mathrm{D}t} + a\nabla\cdot\boldsymbol{v} - a\dfrac{\mathrm{D}s}{\mathrm{D}t} = 2\delta a V_s \\ \dfrac{\mathrm{D}\boldsymbol{v}}{\mathrm{D}t} + \dfrac{a}{\delta}\nabla a - a^2\nabla s = \boldsymbol{V}_m \\ \dfrac{\mathrm{D}s}{\mathrm{D}t} = V_s \end{cases} \tag{1}$$

where t denotes time, γ denotes the ratio of specific heats, $\delta = (\gamma - 1)/2$, and the nondimensional viscous terms V_s and $\boldsymbol{V}_m$ are

$$V_s = \frac{\nabla\cdot\boldsymbol{q} + \nabla\boldsymbol{v}{:}\boldsymbol{T}}{\gamma p} \tag{2}$$

$$\boldsymbol{V}_m = \frac{\nabla\cdot\boldsymbol{T}}{\rho} \tag{3}$$

where p denotes pressure, ρ density, $\boldsymbol{T}$ the stress tensor, and $\boldsymbol{q}$ the heat flux.

The numerical integration of Eqs. (1) is based on the separation of the role of the viscous terms, whose derivatives are discretized by central differencing,[11] from the convective terms, which are treated following the λ scheme[10] by upwind differences, to emphasize the effect of the propagation of signals.

As a consequence, the left-hand sides of Eqs. (1) are reformulated following Ref. 10. The propagation phenomenon is simulated by signals running along four bicharacteristic lines and the streamline direction. In particular, assuming an orthogonal grid and two unit vectors $\boldsymbol{i}$ and $\boldsymbol{j}$, orthogonal to each other and parallel to the coordinate lines at each point, the equations are recast, using the two velocity components $u = \boldsymbol{v}\cdot\boldsymbol{i}$ and $v = \boldsymbol{v}\cdot\boldsymbol{j}$, as

$$\begin{cases} a_t = \delta\left(f_1^x + f_2^x + f_1^y + f_2^y + 2\delta a V_s + a s_t\right) \\ u_t = f_1^x - f_2^x + f_3^y + \boldsymbol{V}_m\cdot\boldsymbol{i} \\ v_t = f_1^y - f_2^y + f_3^x + \boldsymbol{V}_m\cdot\boldsymbol{j} \\ s_t = f_4^x + f_4^y + V_s \end{cases} \tag{4}$$

Presented as Paper 95-2159 at the AIAA 26th Fluid Dynamics Conference, San Diego, CA, June 19–22, 1995; received July 18, 1995; revision received March 26, 1996; accepted for publication March 27, 1996.

*Ph.D., Department of Mechanical and Aeronautical Engineering; currently Postdoctoral Research Assistant, Department of Mechanical and Aeronautical Engineering, Via Eudossiana 18. Member AIAA.

†Associate Professor, Department of Mechanical and Aeronautical Engineering, Via Eudossiana 18. Senior Member AIAA.

where the terms f_p^q indicate the convective contributions along each bicharacteristic line. For instance, f_1^x is the contribution carried along the bicharacteristic λ_1^x to the propagating signal, f_2^x is the contribution along the bicharacteristic λ_2^x, and so on. In particular, they are

$$
\begin{aligned}
f_1^x &= -0.5\lambda_1^x\left[\left(R_1^x\right)_X - v\alpha_X - as_X\right]\\
f_2^x &= -0.5\lambda_2^x\left[\left(R_2^x\right)_X + v\alpha_X - as_X\right]\\
f_3^x &= -\lambda_3^x(v_X + u\alpha_X)\\
f_4^x &= -\lambda_3^x s_X
\end{aligned}
\tag{5}
$$

$$
\begin{aligned}
f_1^y &= -0.5\lambda_1^y\left[\left(R_1^y\right)_Y + u\alpha_Y - as_Y\right]\\
f_2^y &= -0.5\lambda_2^y\left[\left(R_2^y\right)_Y - u\alpha_Y - as_Y\right]\\
f_3^y &= -\lambda_3^y(u_Y - v\alpha_Y)\\
f_4^y &= -\lambda_3^y s_Y
\end{aligned}
\tag{6}
$$

where α in the preceding equations and G in the following equations are the metric coefficients of the mapping between the computational (X, Y) and the physical (x, y) planes, as defined in Ref. 10. The other terms appearing in Eqs. (5) and (6) are defined as

$$\lambda_1^x = G(u + a), \qquad \lambda_2^x = G(u - a), \qquad \lambda_3^x = Gu \tag{7}$$

$$\lambda_1^y = G(v + a), \qquad \lambda_2^y = G(v - a), \qquad \lambda_3^y = Gv \tag{8}$$

$$R_1^x = a/\delta + u, \qquad R_2^x = a/\delta - u \tag{9}$$

$$R_1^y = a/\delta + v, \qquad R_2^y = a/\delta - v \tag{10}$$

The integration of Eq. (4) is performed following the two-level explicit scheme, having second-order accuracy, described in detail in Ref. 10 and extended to viscous flows in Ref. 11.

Shock-Fitting Technique

In any fitting technique the shock position is defined by its intersection with the computational grid. Following nomenclature and definitions introduced by Moretti, x shock and y shock denote the intersections of the shock with the $Y = \text{const}$ and $X = \text{const}$ coordinate lines, respectively (Fig. 1). Depending on the flow conditions, two kinds of x shock are possible with higher pressure either on its left or on its right side. Analogously two kinds of y shock may exist. The variables on the low-pressure side of the shock are denoted with the subscript A, whereas the subscript B indicates the variables on the high-pressure side.

All of the information about the shock points is stored in arrays at random. This means that the first shock point detected is placed in the first place of the arrays, the second at the second, and so on, regardless of their location in the flowfield. For each shock point the following indices are defined as follows: 1) node (n_s, m_s): the node on the left-hand side of an x shock or below a y shock; 2) index JI: to distinguish x shocks from y shocks, and shocks having or not the high-pressure side at (n_s, m_s): JI $= 0$, x shock with high-pressure side at (n_s, m_s); JI $= 1$, x shock with low-pressure side at (n_s, m_s); JI $= 2$, y shock with high-pressure side at (n_s, m_s); and JI $= 3$, y shock with low-pressure side at (n_s, m_s).

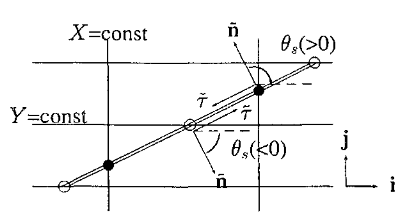

Fig. 1 Shock points: ○, x shock and ●, y shock.

It is also useful to introduce for each shock point 1) a frame of reference aligned with the shock and defined by two unit vectors, $\tilde{n}$ having the direction of the shock normal and $\tilde{\tau}$ parallel to the shock (Fig. 1); 2) the absolute velocity components $\tilde{u} = \boldsymbol{v} \cdot \tilde{n}$, and $\tilde{v} = \boldsymbol{v} \cdot \tilde{\tau}$; and 3) the following variables: a) position (X_s, Y_s); b) angle θ_s: angle of the shock normal $\tilde{n}$ to the unit vector $\boldsymbol{i}$, positive counterclockwise (Fig. 1) (the orientation of $\tilde{n}$ is different for x and y shocks and such that $\cos\theta_s > 0$ for an x shock and $\sin\theta_s > 0$ for a y shock); c) velocity of the shock front $W_s\tilde{n}$; d) shock Mach number M_s: Mach number of the flow normal to the shock, in a reference system moving with the shock; it represents the shock strength; and e) $u_A, v_A, a_A, s_A, u_B, v_B, a_B, s_B$: integration variables on the low- and high-pressure sides of the shock, respectively.

As the shock points are stored at random (with a storing index J), each mesh node is marked to easily identify the neighborhood of each shock point. In particular, an array JSX is set equal to zero in all of the mesh nodes, except in the nodes having on their left side an x shock with index J, where it is set equal to J. Similarly, a null array JSY is set equal to J in the mesh nodes, which have a y shock below with index J.

A major difference between the present and the classical approach is relevant to the shock points considered. Indeed, in Ref. 5 only x shocks having $0 < \theta_s < 45$ deg and y shocks having $45 < \theta_s < 135$ deg were considered as shock points. Such a limitation of the number of shock points allows some simplification in updating the mesh nodes on the high-pressure side of a shock point and in the displacement of the shock. Unfortunately, it also leads to topological complications in the computation of the shock angle, particularly when the flowfield displays shocks close to each other. Because of this problem the analysis in the neighborhood of a shock point has been worked out in greater detail.

The approach presented here considers as shock points all intersections between shocks and coordinate lines. It allows a better understanding of the geometric shape of the shock, especially when more than one shock occurs in a region of the flowfield or when two shocks interact with each other. Each time iteration of the integration process can be organized in six main steps: 1) integration of the equations over all of the mesh nodes, according to the λ scheme; 2) detection of the formation of new shocks; 3) calculation of the local slope of the shocks; 4) enforcement of the Rankine–Hugoniot jump conditions between the two sides of each shock point; 5) displacement of the shock points, according to the velocity of propagation of the shock front; and 6) introduction of connecting shock points.

Integration of the Equations

The variables are computed following the upwind rules of the classical λ scheme. A careful handling of the calculation in the nodes about shock points is needed to avoid differentiating across discontinuities. In fact, updating of the variables behind the shock is provided by the Rankine–Hugoniot jump conditions, as will be shown in the following. Similar care applies to the treatment of the viscous terms, which is thus based on one-sided differencing at nodes with shock points in the neighborhood. Indeed, if differentiation across shock points is not avoided, the computation of the diffusive phenomenon would be locally overestimated.

Detection of New Shocks

The detection of new shock points is based on the formation of shocks by coalescence of waves. Splitting the two-dimensional problem into two one-dimensional problems, one along each coordinate line, one can perform the detection by analyzing the behavior of the bicharacteristics $\lambda_{1,2}^x$ and $\lambda_{1,2}^y$ as functions of X and Y, respectively. For example, a new x shock point will be located where $\mathrm{d}\lambda_1^x/\mathrm{d}X$ displays a relative minimum and is negative.[7] A further check on pressure avoids the detection of contact discontinuities and physically unrealistic expansion shocks.

Calculation of the Local Shock Angle

The calculation of the local shock angle θ_s is the most critical part of the fitting procedure. Indeed, it affects the whole shock evaluation, and in particular the prediction of the motion of the shock, crucial in unsteady flow analysis.

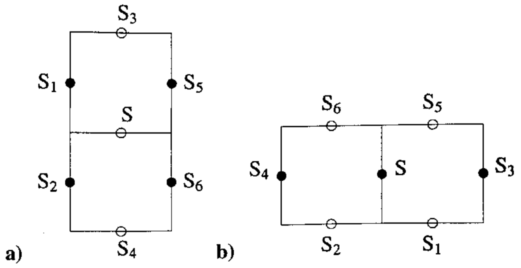

Fig. 2 Possible shock points around a) an x shock and b) a y shock.

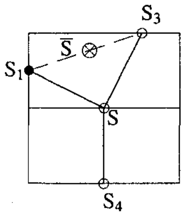

Fig. 3 Triple shock point.

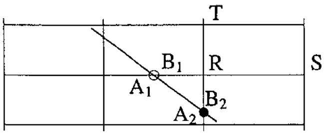

Fig. 4 Enforcement of the jump conditions for an oblique shock.

A precise evaluation of the angle can be achieved by connecting a shock point with its neighboring ones.[5] Since problems may arise when shocks are close to each other, the present procedure relies on a careful analysis to recognize the neighboring shock points that belong to the same shock. The thorough logic needed is described in the following for an x shock, by using the sketch of Fig. 2a as reference. The y shocks are treated similarly, following the sketch in Fig. 2b.

The shock crosses the x-coordinate line in S (Fig. 2a) and must cross the mesh at least at one other point S_i ($i = 1, \ldots, 6$). Therefore, isolated shock points S, which do not display any shock point like S_i, cannot exist and must be removed. Indeed, they may appear only as a consequence of numerical inaccuracies or as a part of a weakened shock.

Then, the existing shock points S_i are analyzed to see whether they are compatible with S. For example, if S has JI = 1, possible shock points compatible with it must have JI = 1 in S_3 and S_4, JI = 2 in S_2 and S_5, and JI = 3 in S_1 and S_6. A further check removes the shock points that have no compatible shocks in their neighborhood. After this preliminary cleaning of spurious shock points, the calculation of θ_s is performed differently for an ordinary or a triple or a multiple shock point as defined next.

Ordinary Shock Points

Ordinary shock points are defined as shock points S with no more than two shock points in their neighborhood, one (S_i, $i = 1, 3, 5$) in the mesh above and/or one (S_j, $j = 2, 4, 6$) in the mesh below. In the general case, the connection of the shock points around S used to compute θ_s should be carried out following a physical criterion based on the domain of dependence. From this point of view two cases are possible:

1) Sup-shock when $|\tilde{v}_A| > a_A$ and $|\tilde{v}_B| > a_B$ ($\tilde{v}_A = \tilde{v}_B$): In this case no signal can propagate upstream in the direction tangential to the shock, being the flow supersonic in that direction at both sides of the shock. As a consequence, no S_i that is downstream of S along the shock can affect the computation of θ_s in S. Therefore, only the shock point located upstream of S is used to compute θ_s, and only if it does not exist is the shock point downstream considered. Anyhow, only one S_i is used, and θ_s is computed taking $\tilde{\boldsymbol{n}}$ as the normal to the direction S–S_i.

2) Sub-shock when $|\tilde{v}_A| < a_A$ or $|\tilde{v}_B| < a_B$ ($\tilde{v}_A = \tilde{v}_B$): In this case θ_s is computed taking $\tilde{\boldsymbol{n}}$ as the normal to the direction S_i–S_j, if both S_i and S_j exist. If one of them does not exist, $\tilde{\boldsymbol{n}}$ is taken as the normal to the direction S–S_i (or S–S_j).

Triple Shock Points

An x shock is defined as a triple shock point if either two of S_1, S_3, and S_5 or two of S_2, S_4, and S_6 exist (Fig. 2a). Let us consider the example of Fig. 3. If S, S_4, and S_3 have the high-pressure side on the right, and S_1 on the upper side, then S is actually a triple point and requires a specific treatment, whereas S_1 and S_3 are ordinary shock points. Following the technique proposed in Ref. 7, θ_s is computed taking $\tilde{\boldsymbol{n}}$ as the normal to the direction $\bar{S}$–S_4, where $\bar{S}$ is the middle point of the line S_1–S_3.

Multiple Shock Points

During the computation, particularly in the case of transient flows, it may happen that many shock points are close to each other. If there are both two or three compatible shock points above S and two or three compatible shock points below S (Fig. 2a), θ_s is obtained with a procedure similar to that used for triple points. Accordingly, $\tilde{\boldsymbol{n}}$ is taken as the normal to the direction $\bar{S}$–$\bar{\bar{S}}$, where $\bar{S}$ is the geometric mean of the existing upper points S_1, S_3, S_5, and $\bar{\bar{S}}$ is the geometric mean of the existing lower points S_2, S_4, S_6.

Enforcement of the Jump Conditions

The values of the variables in the mesh node on the low-pressure side of the shock and the value of one Riemann variable, Eqs. (9) and (10), in the mesh node on the high-pressure side have been computed correctly in the first step.[10] On the other hand, the values on the high-pressure side of the shock are updated by means of the Rankine–Hugoniot relations once the shock strength M_s, defined as

$$M_s = \frac{|\tilde{u}_A - W_s|}{a_A} \tag{11}$$

has been computed.

To evaluate M_s, a new variable Σ can be introduced,[3] computed from the variables on the low-pressure side and the Riemann variable on the high-pressure side of the shock as

$$\Sigma = \frac{(a_B + \delta|\tilde{u}_A - \tilde{u}_B|)}{a_A} \tag{12}$$

Since Σ can also be expressed as a monotonic increasing function of M_s,

$$\Sigma = \frac{\sqrt{(\gamma M_s^2 - \delta)(1 + \delta M_s^2)} + \delta(M_s^2 - 1)}{(1 + \delta)M_s} \tag{13}$$

the shock strength M_s is obtained by inverting Eq. (13). Nevertheless, if Σ is less than a threshold value (typically 1.02–1.05),[7,9] the shock is weak enough to be considered an isentropic compression, and therefore the shock point is removed. The values of the variables in the mesh node on the high-pressure side of the shock are then updated by interpolation between the values on the shock and those on the next node.

This classical procedure is adopted except when updating a mesh node R located on the high-pressure side of two shock points: an x shock and a y shock (Fig. 4). In this case, a first interpolation is done between B_1 and S and a second between B_2 and T. The updated values in R are taken as the weighted mean of the two sets of interpolated values, where the weight Ω_s is defined as

$$\Omega_s = \begin{cases} \cos\theta_s & \text{for} \quad x \text{ shocks} \\ \sin\theta_s & \text{for} \quad y \text{ shocks} \end{cases} \tag{14}$$

to give more relevance to shock points lying on the coordinate line closer to the shock normal.

Displacement of the Shock

The displacement of the shock in the direction $\tilde{\boldsymbol{n}}$ is $W_s \Delta t$, with W_s computed by Eq. (11). Therefore an x shock moves a length

$$\Delta x = \frac{W_s \Delta t}{\cos\theta_s} \tag{15}$$

along the coordinate line Y = const (Fig. 5). If the x shock in its displacement passes over a mesh node, the values at that node are

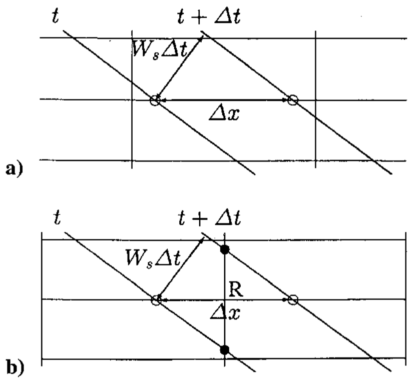

Fig. 5 Displacement of an x shock.

replaced by the values on the side of the shock that lies between the new position of the shock point and the node.

A procedure different from the classical one is needed when two shock points, an x shock and a y shock, pass over the same mesh node (Fig. 5b). The values in the mesh node R traversed by the pair of shock points are updated with the shock values that are taken as the mean values of the two shocks, weighted by Ω_s defined in Eq. (14). Nevertheless, since the displacement Δx is obtained from Eq. (15) dividing by $\cos\theta_s$, numerical inaccuracies may occur when the shock is almost parallel to a coordinate line. Because of such inaccuracies, it may happen that only one of the two shock points passes over R. In this case the movement of the shock point having greater Ω_s is assumed as correct, whereas the other shock point is removed. This last shock point will be replaced by a new connecting shock point in step 6, as shown in the following.

Introduction of Connecting Shock Points

At times, shock points are lost as a result of numerical inaccuracies in the detection phase or removal of points that appear to be too weak or incorrectly located. In these cases, such shock points must be reintroduced, because they are needed to define the shock geometry and to assure its smoothness.

A first possible situation concerns two x shocks in S and S_B having same JI (Fig. 6a). If a y shock in S_5 is missing, a new point S_5 will be introduced to connect S_B and S. Nevertheless, it must be noticed that the connection between shock points belonging to different shock waves and the overcrowding of shock points must be avoided. Therefore, the shock point in S_5 is inserted only if all of the following four conditions occur: 1) S or S_B has $\theta_s < 0$; 2) there are not both S_U (and/or S_4) compatible with S and S_R (and/or S_6) compatible with S_B; indeed, if this is not true, S and S_B should belong to different shocks and must not be connected by S_5; 3) there are not both S_U and S_2; otherwise the addition of S_5 would create a situation of a node surrounded by four shock points, thus impossible to compute; and 4) there are not both S_R and S_8, for the same reason just stated.

Similar considerations hold when two shock points to be connected are S and S_A, instead of S and S_B. Finally, an analogous procedure is used to insert an x shock between two y shocks.

Another typical situation where connecting shock points have to be inserted is shown in Fig. 6b. If there are two shock points, S having JI = 0 (or 1) and S_A having JI = 3 (or 2), but S_B is missing, the latter must be introduced. Nevertheless, before connecting S and S_A with the y shock S_B having the same JI as S_A, it must be checked if S and S_A can belong to the same shock. This is not true if one of the following conditions occurs: 1) there is S_1; 2) there are both S_2 and S_3; 3) S has $\theta_s > 0$ and S_A has $\theta_s < \pi/2$; and 4) there is S_4 and it does not have the same JI as S_A.

Further considerations concern very particular situations, like the triple point shown in Fig. 6c, when two x shocks S_A and S_B have the same JI, a y shock is in S, whereas the y shock in S_4 is missing. In this case the y shock S_4, having the same JI as S, has to be inserted only if there are not the shock points S_1, S_2, S_3, and S_5, and S cannot be connected to other x shocks like S_6 or S_7. Of course, the preceding procedures are analogously applied in all of the symmetrical situations.

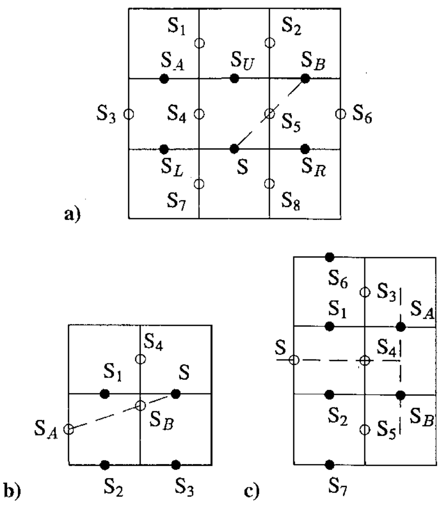

Fig. 6 a) Connection of x shocks; b) connection between x and y shocks; and c) connection of two x shocks and a y shock close to a triple point.

Contact Discontinuities

Contact discontinuities (CD) are fitted following a procedure similar to the shock fitting, but only CDs existing at the beginning of the computation are considered, without performing any detection. Therefore, only four more steps have to be added to the preceding six steps of the integration technique: 7) calculation of the local slope of the CD, 8) enforcement of the CD relations across the discontinuity, 9) displacement of the CD, and 10) introduction of connecting CD points.

A set of indices and variables identical to that for a shock point is introduced for a CD point, and the calculation of the local slope, the displacement, and the introduction of connecting points follow the same procedure as for the shocks. The main difference concerns the enforcement of the relations across the CD. Only two kinds of CD are defined: x-CD classified with JI = 0 and y-CD classified with JI = 1. Moreover, the subscript A denotes the left (lower) side and the subscript B the right (upper) side.

The value of variables at the mesh nodes near a CD computed in the first integration step are not correct on either side of the discontinuity. But, in a frame of reference moving with the CD, the variables in Eq. (9), R_1^x in the mesh node at the left side of an x-CD and R_2^x in the mesh node at its right side, are computed correctly. As a consequence, the CD relations

$$\tilde{u}_A = \tilde{u}_B = W_c \tag{16}$$

$$p_A = p_B \tag{17}$$

along with the definitions

$$a_A + \delta\tilde{u}_A = \delta\left(R_1^x\right)_A \tag{18}$$

$$a_B - \delta\tilde{u}_B = \delta\left(R_2^x\right)_B \tag{19}$$

provide the equations for the calculation of the unknowns $\tilde{u}_A$, $\tilde{u}_B$, a_A, a_B, and W_c. The mesh nodes on the left- and right-hand sides of the discontinuity are updated by interpolation between these values and the ones at the next nodes. The values $\tilde{v}_A$, s_A, and $\tilde{v}_B$, s_B are independent of each other. They are correctely computed in the first step of the integration, since they are not affected by signals propagating across the CD.

Results

Many classical test cases have been performed to provide a broad validation of the proposed fitting technique.

Regular Reflection

The steady inviscid regular reflection of an oblique shock is presented as the first test case to assess the accuracy of the method.

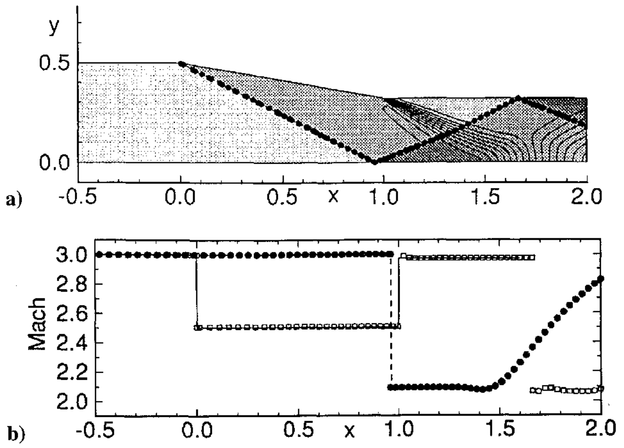

Fig. 7 Steady inviscid regular reflection of an oblique shock: a) present computation of Mach number isocontours (ΔM = 0.05) and shock points (●); and b) present and analytical wall Mach number solution: □, present, upper wall; ●, present, lower wall; ——, analytical, upper wall; and – – –, analytical, lower wall.

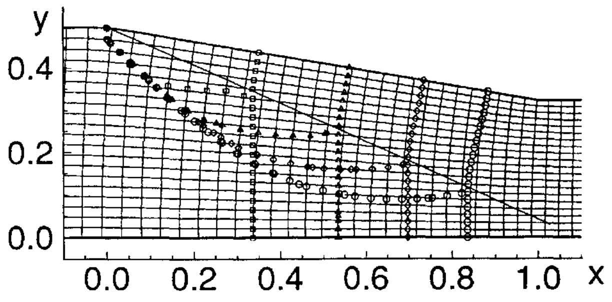

Fig. 8 Unsteady inviscid Mach reflection: □, △, ◇, and ○, computed shock points at different times and ——, measured position of the triple point.[12]

A supersonic flow with a Mach number $M = 3$ enters a two-dimensional plane duct whose geometry displays two regions with constant area sections joined through a ramp of 10-deg slope (Fig. 7a) and having a contraction ratio of 0.65. Numerical results computed with a 70×20 grid are shown in Fig. 7a through Mach number isocontours and shock points fitted. In the region not affected by wave interactions (i.e., $x < 1.4$ along the axis and $x < 1.7$ along the wall), it is possible to compute the analytical solution by means of oblique shock and Prandtl–Meyer expansion relations. The comparison is shown in Fig. 7b for the Mach number along wall and axis and indicates a good agreement between the analytical and numerical solutions.

Mach Reflection

The preceding geometry has been also considered to validate the numerical handling of triple points in transient flows. A plane shock ($M_s = 6.69$) followed by an inviscid supersonic flow ($M = 1.75$) moves from the left in quiescent air. As it enters the converging ramp, a simple Mach reflection occurs. Before the reflected shock reaches the lower wall, the flow behaves as in an unbounded field, and the solution is pseudostationary, i.e., similar to itself in time, with the triple point moving along a straight line. The slope of this line cannot be predicted analytically because of the complex flowfield behind the shock, but its value was measured experimentally[12] as 24.5 deg. The comparison between the computed solution and experimental evidence is shown in Fig. 8: it allows one to verify the excellent numerical prediction of the triple point movement, in simple unsteady problems.

Shock Implosion

The next test case concerns the inviscid solution of the flowfield relevant to a cylindrical converging shock wave. This test allows the assessment of the capability of the fitting technique to predict the movement of flow discontinuity fronts forming any angle with the coordinate lines.

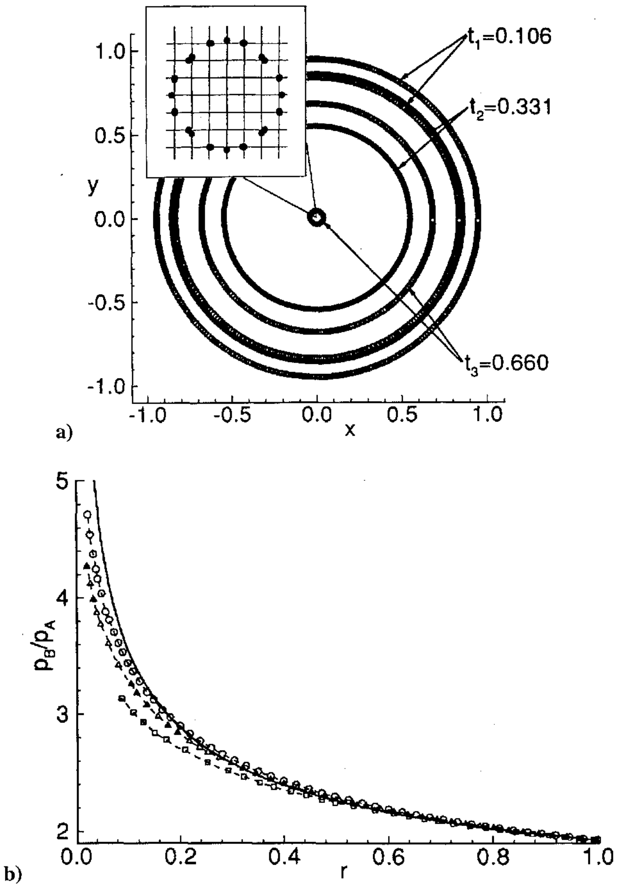

Fig. 9 Inviscid simulation of the propagation of a converging shock wave: a) computed shock (●) and contact discontinuity (○) at three different times; and b) convergence of the numerical solution (□, Δx = 0.0333; △, Δx = 0.0167; and ○, Δx = 0.0083) towards the analytical one[13] (——).

The flow starts at $t = 0$ by the rupturing of a cylindrical diaphragm that separates two regions of quiescent air at the same temperature but at different pressures. In particular, the pressure on the external side of the cylindrical diaphragm is four times greater than on the internal side. The flow that takes place has a structure characterized by a cylindrical converging shock wave followed by a converging contact discontinuity, and by diverging expansion waves. The numerical simulation starts right after the diaphragm removal, assuming the diaphragm radius as the nondimensionalization length, and as initial conditions the one-dimensional shock-tube analytical solution, with radial effects considered negligible. Both shock and contact discontinuity have been fitted. The calculation has been performed on a Cartesian grid, with the origin of the frame of reference placed on the axis of the cylindrical diaphragm. The choice of such a grid allows a clear evaluation of the capability of the method to handle discontinuities having any orientation with respect to the grid lines.

In Fig. 9a the position of the discontinuities computed at three different times is shown. The number of shock or CD points describing the discontinuities in the figure is 28 for the smaller and 580 for the larger. An enlargement of the smaller distribution of shock points with the grid superimposed is shown as an inset in the same figure; it provides an indication of the capability of the technique to predict the correct shape even with a limited amount of shock points and independently of the angle between shock and grid lines.

To assess the accuracy of the calculation, Fig. 9b shows the comparison between numerical solutions and analytical predictions[13] for the shock strength (p_B/p_A) as a function of the distance r from the origin. The grid refinement shows that the numerical solutions converge towards the analytical one as the resolution increases. Of course, the numerical solution degenerates in proximity of the origin, but closer and closer to it as the mesh size is reduced.

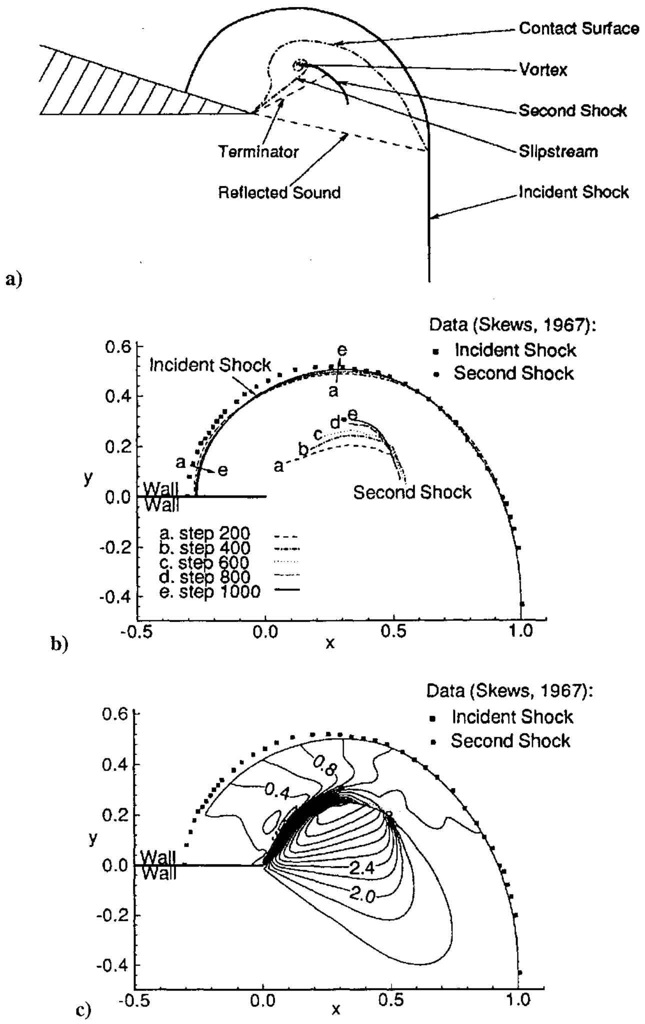

Fig. 10 a) Features of the shock diffraction pattern[14] and b) and c) present inviscid simulation of a diffraction around a 180-deg corner: b) evolution of the computation compared with experiments[14] and c) Mach number isocontours.

Shock Diffraction

The diffraction of a shock around an edge is used as another validation test. Also in this case the solution has a pseudostationary character,[14] and therefore it allows an easy validation of the method for a flow transient more complex than the previous ones. A plane shock ($M_s = 4$) followed by a uniform supersonic flow ($M = 1.55$) moves from the left along a straight wall in quiescent air; as it reaches the wall edge, it is diffracted, generating the complex flow structure studied in Ref. 14 (Fig. 10a). To make the test more meaningful, the less favorable condition, with a diffraction around a 180-deg corner, has been considered. The flow structure, featuring contact discontinuity, slipstream, and vortex, is well reproduced by the inviscid numerical solution, as shown by the Mach number isocontours (Fig. 10b).

The comparison between this numerical solution and the experimental data by Skews[14] is shown in Fig. 10c. The numerical solution gives a good prediction of both the profile of the incident shock and the location of the left end of the second shock, whose corresponding experimental position is indicated by a filled circle.

A significant indication about the accuracy of the method is provided by the analysis of the evolution in time of the solutions, normalized by the distance covered by the shock along the abscissas. Indeed, as time elapses, the number of mesh nodes between the edge and the incident shock increases, and since the solution is similar to itself, the numerical transient acts as an integration with increasing number of mesh nodes. As the grid becomes finer, the profile of the second shock converges towards a final position, in good agreement with the experimental data. On the contrary, the incident shock, which is weakly affected by the flow evolution behind it, maintains its similarity, independently of the number of shock points.

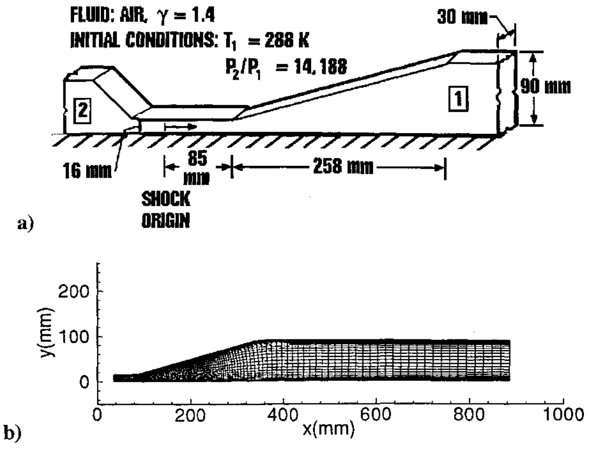

Fig. 11 a) Geometry of the 16-deg nozzle used for the nozzle startup viscous simulation and b) computational grid.

Wind Tunnel Startup

Finally, a viscous unsteady test has been carried out by simulating the experiments of a transient nozzle airflow performed by Opalka.[15] The experimental data reported are optical records of the startup process in a two-dimensional plane nozzle, having the convergent and divergent sections connected by a constant area throat duct (Fig. 11a). At the right-hand side of the divergent section, the duct features a long constant area channel (about 1 m long) so as to delay the arrival of reflections from its end.[15] The flow starts at $t = 0$ after the rupturing of a diaphragm, located at $x = 0$ in the throat duct, which separates two regions of quiescent air. The high-pressure region, on the left-hand side, is at reservoir conditions, temperature $T_c = 288$ K and pressure $p_c = 14$ bar, whereas the low-pressure region, on the right side, is at ambient conditions, $T_a = 288$ K and $p_a = 1$ bar.

Linear dependence on temperature is assumed for viscosity, $\mu/\mu_r = T/T_r$, using as reference the air values, $\mu_r = 1.786 \times 10^{-5}$ kg m^{-1} s^{-1} and $T_r = 288$ K; thermal conductivity is obtained as a function of viscosity, Prandtl number, and specific heat at constant pressure. The computational domain and the 120 × 40 grid used are shown in Fig. 11b, where the minimum distance between the nodes closer to the walls in normal direction is 5.9×10^{-6} m.

Initially, just after the removal of the diaphragm, the boundary layer is not developed yet, and therefore the solution follows the classical shock tube pattern: 1) a strong incident shock wave moves rapidly towards the low-pressure side, 2) a contact discontinuity follows the incident shock, and 3) an expansion fan moves towards the high-pressure side. To avoid the presence of the shock and CD points in a single mesh, the numerical simulation does not start at $t = 0$ but at 0.139 ms, initialized with the Eulerian one-dimensional shock-tube solution. Moreover, the location of the inlet section is such that neither the expansion tail nor the expansion front reflected by the converging section significantly affects the solution in the computational domain during the period of time analyzed. As a consequence of the preceding assumptions, supersonic boundary conditions have been enforced at the inflow, along with adiabatic wall and nonreflecting outflow.

The computed flowfield at three different times is shown by Mach number isocontours in Figs. 12a–12c. At $t = 1.26$ ms, the contact discontinuity is clearly visible at the end of the divergent section. It is followed by the recompression shock and by the upper and lower separation zones, which yield weak oblique compressions in the core flow (Fig. 12a). As shown in Fig. 12b, at $t = 1.76$ ms the separated zones are extended downstream, and compressions, produced by the interactions between the supersonic flow and the separation surfaces, cross each other in the core flow. Finally, at $t = 2.26$ ms the flow structure is characterized by two separated zones, by oblique and reflected compressions, and by further recompression shocks (Fig. 12c).

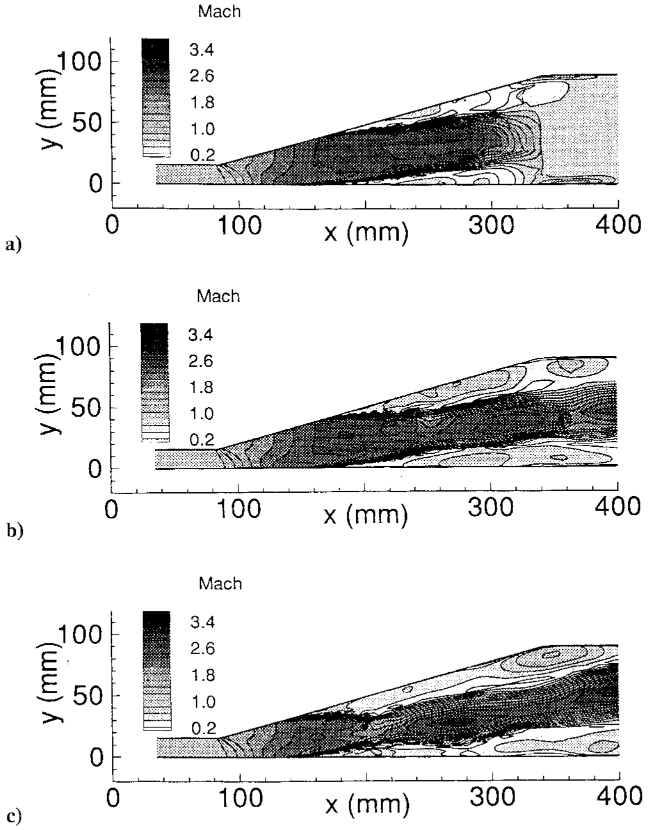

Fig. 12 Mach number isocontours ($\Delta M = 0.2$) for the nozzle startup viscous simulation: t = a) 1.26, b) 1.76, and c) 2.26 ms.

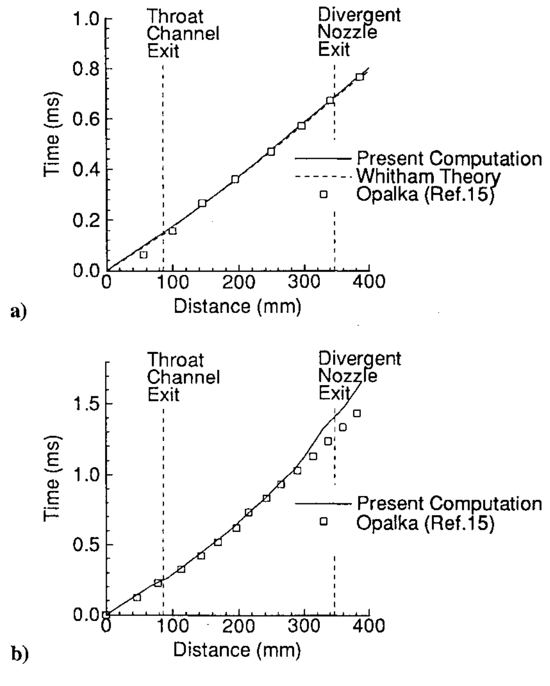

Fig. 13 Time evolution of a) incident shock and b) contact discontinuity position obtained from present viscous computation, experiments,[15] and Whitham theory.[16]

The comparison between the numerical results and the experiments of Ref. 15, which considers also the delay time for shock formation measured by Opalka as 0.06 ms, shows the capability of the method to give a qualitative prediction of a complex viscous transient flow. On the contrary, as the quality of the optical records is very poor, a quantitative comparison of the flow structures seems questionable.

However, a quantitative assessment of the prediction can be achieved by analyzing the movement of the fronts of the incident shock (Fig. 13a) and of the contact discontinuity (Fig. 13b). The computed locations of these discontinuities display very good agreement with the experimental evidence,[15] particularly in the first phase, when they propagate downstream without substantial interference with the regions dominated by the separated flow. In a sense, their propagation is driven by Eulerian laws, and in fact the incident shock evolution agrees also with that obtained by using the two-dimensional theory of Whitham.[16] Later on, small differences occur for the CD; indeed, in this second phase the separated zone and the CD display a more extended interacting zone, and the irregular shape of the CD makes less certain the determination of its position by a single abscissa.

Conclusions

A natural evolution of Moretti's classical shock-fitting technique has been carried out and validated by means of specific test cases. In particular, it has been applied to transient flows, where the fitting and tracking of discontinuities show distinct advantages in comparison with other methods that need cumbersome adaptive grid techniques and/or high-order capturing schemes. Compared with the previous classical technique, the new version appears to be more robust and capable of treating complex flowfields, including interactions among flow discontinuities.

The proposed fitting technique can also be implemented in codes that integrate the equations in smooth regions of the flowfield with approaches different from that of the λ scheme.

Acknowledgments

This work was partially performed under a contract with Deutsche Aerospace (n. R-5598-8687 R) within the framework of the European Launcher Investigation and Technology Effort study financed by the European Space Agency. Partial support by Agenzia Spaziale Italiana, Contract 94-RS-29, is also acknowledged. The authors want to thank G. Moretti for his stimulating support and B. Favini for helpful discussions.

References

[1] Moretti, G., "Thoughts and Afterthoughts about Shock Computations," Dept. of Aerospace Engineering and Applied Mechanics, Polytechnic Inst. of Brooklyn, PIBAL Rept. 72-37, Brooklyn, NY, Dec. 1972.

[2] Moretti, G., "Circumspect Exploration of Multidimensional Imbedded Shocks," *AIAA Journal*, Vol. 14, No. 7, 1976, pp. 894–899.

[3] Moretti, G., and Di Piano, M. T., "An Improved Lambda-Scheme for One-Dimensional Flows," NASA CR 3712, Sept. 1983.

[4] Moretti, G., "A Numerical Analysis of Muzzle Blast Precursor Flow," *Computer and Fluids*, Vol. 10, No. 1, 1982, pp. 51–86.

[5] Moretti, G., "Efficient Calculations of 2D Compressible Flows," *Advances in Computer Methods for PDE*, Vol. 6, IMACS, New Brunswick, NJ, 1987, pp. 60–66.

[6] Moretti, G., "Computation of Flows with Shocks," *Annual Review of Fluid Mechanics*, Vol. 19, 1987, pp. 313–337.

[7] Moretti, G., and Valorani, M., "Detection and Fitting of Two-Dimensional Shocks," *Notes on Numerical Fluid Mechanics*, Vol. 20, Vieweg, Braunschweig, Germany, 1988, pp. 239–246.

[8] Nasuti, F., and Onofri, M., "Numerical Study of Unsteady Compressible Flows by a Shock-Fitting Technique," *Lecture Notes in Physics*, Vol. 453, Springer–Verlag, Berlin, 1995, pp. 407–412.

[9] Hartwich, P. M., "Comparison of Coordinate Invariant and Coordinate Aligned Upwinding for the Euler Equations," *AIAA Journal*, Vol. 32, No. 9, 1994, pp. 1791–1799.

[10] Moretti, G., "A Technique for Integrating Two-Dimensional Euler Equations," *Computer and Fluids*, Vol. 15, No. 1, 1987, pp. 59–75.

[11] Moretti, G., Marconi, F., and Onofri, M., "Shock Boundary Layer Interactions Computed by a Shock Fitting Technique," *Lecture Notes in Physics*, Vol. 414, Springer–Verlag, Berlin, 1993, pp. 345–350.

[12] Ben-Dor, G., *Shock Wave Reflection Phenomena*, Springer–Verlag, New York, 1992, p. 75.

[13] Chisnell, R. F., "The Motion of a Shock Wave in a Channel, with Application to Cylindrical and Spherical Shock Waves," *Journal of Fluid Mechanics*, Vol. 2, May 1957, pp. 286–298.

[14] Skews, B. W., "The Perturbed Region Behind a Diffracting Shock Wave," *Journal of Fluid Mechanics*, Vol. 29, Sept. 1967, pp. 705–719.

[15] Opalka, K. O., "Optical Studies of the Flow Start-Up Processes in Four Convergent Divergent Nozzles," U.S. Army Ballistic Research Lab., TR BRL-TR-3215, Aberdeen Proving Ground, MD, March 1991.

[16] Whitham, G. B., "A New Approach to Problems of Shock Dynamics—Part I," *Journal of Fluid Mechanics*, Vol. 2, March 1957, pp. 145–171.